

# Environment and Person Independent Activity Recognition with a Commodity IEEE 802.11ac Access Point

Francesca Meneghelli<sup>\*\*</sup>, Domenico Garlisi<sup>†</sup>, Nicolò Dal Fabbro<sup>\*</sup>, Ilenia Tinnirello<sup>†</sup>, Michele Rossi<sup>\*‡</sup>

**Abstract**—Here, we propose an original approach for human activity recognition (HAR) with commercial IEEE 802.11ac (WiFi) devices, which generalizes across different persons, days and environments. To achieve this, we devise a technique to extract, clean and process the received phases from the channel frequency response (CFR) of the WiFi channel, obtaining an estimate of the Doppler shift at the receiver of the communication link. The Doppler shift reveals the presence of moving scatterers in the environment, while not being affected by (environment specific) static objects. The proposed HAR framework is trained on data collected as a person performs four different activities and is tested on unseen setups, to assess its performance as the person, the day and/or the environment change with respect to those considered at training time. In the worst case scenario, the proposed HAR technique reaches an average accuracy higher than 95%, validating the effectiveness of the extracted Doppler information, used in conjunction with a learning algorithm based on a neural network, in recognizing human activities in a subject and environment independent fashion.

**Index Terms**—sensorless sensing, device-free, WiFi sensing, human activity recognition, neural networks, machine learning, CSI, CFR, IEEE 802.11ac.

## I. INTRODUCTION

Human activity recognition (HAR) systems are key elements of emerging applications for smart buildings. Among others, they can be profitably used to optimize the buildings' energy consumption, implement alert systems, and provide platforms for smart entertainment. Also, in a residential scenario, they enable solutions for elderly care, to promptly detect critical situations or, for assisted living, to support physically impaired people in their daily activities [1].

In this work, we present a device-free HAR system for indoor spaces, which relies upon the analysis of scattered WiFi signals. A commercial-off-the-shelf (COTS) WiFi router is used as a sensor to obtain information of moving targets. The Doppler information at the receiving end of the WiFi link is extracted and utilized to concoct an environment-and person-independent learning based algorithm that reliably detects human activities.

Several technologies can serve as sensors for HAR. The most accurate approach relies on wearable devices, such as inertial measurement units (IMUs), smartphones or smart-watches [2]. These, analyze the changes in the accelerometer

and gyroscope data to recognize human movements. However, they require the user to carry along the monitoring device, thus limiting their applicability. For this reason, device-free HAR systems are often preferred. Among these, camera based solutions have been widely investigated and adopted, but they are highly environment dependent as either obstacles in the field of view or low light conditions can heavily impact their performance [3]. Moreover, their use poses privacy issues, as the subjects are clearly identifiable. As an alternative, detection and ranging devices based on radio waves (RADAR) and light beams (LIDAR) are emerging [4]. With them, properly designed signals are irradiated and their reflections are analyzed to infer human presence and activities [5].

In the last decade, since the pioneering work of Adib and Katabi [6], wireless signals of opportunity have been extensively researched as a means to perform device-free localization and activity recognition tasks, including pattern and gesture recognition, and even estimating biological signals at distance, such as the respiration rate or the heartbeat [7]. In this respect, WiFi signals are particularly appealing, due to the high availability of WiFi enabled devices in most residential and working spaces [8]. While active sensing techniques allow localizing and following a user as she/he carries along a WiFi-connected device, passive sensing approaches obtain such information by monitoring the changes in the WiFi channel, where users act as intermediate scatterers that modify the channel frequency response (CFR) [9].

In the present work, we exploit an IEEE 802.11ac router to perform device-free HAR. Human movement data is extracted from the channel state information (CSI), a frequency estimate of the radio channel describing how the signal changes as it propagates from the transmitter to the receiver. Channel estimation is continuously performed by WiFi routers for communication purposes, and specific tools allow gathering such information from COTS devices, exploiting them for environmental sensing. So far, many approaches have been presented in the literature, e.g., [8], [9]. However, we stress that, while they work well within the specific physical environment and conditions for which they were trained, they are not able to reliably recognize human activities across different scenarios, days or with different persons, without being re-trained with the new data. That is, they fall short in generalizing across persons and environments.

In this work, we tackle this open issue by considering the Doppler effect measured at the receiver as persons move within the environment. This Doppler shift reveals the velocities of movement of the scattering points during the transmission

<sup>\*</sup>Corresponding author.

<sup>\*</sup>Department of Information Engineering (DEI), University of Padova, via Gradenigo 6/b, 35131, Padova, Italy. (e-mail: {name.surname}@dei.unipd.it)

<sup>†</sup>Department of Engineering, University of Palermo, Viale delle Scienze, edificio 7, 90128, Palermo, Italy. (e-mail: {name.surname}@unipa.it)

<sup>‡</sup>Department of Mathematics “Tullio Levi-Civita”, via Trieste 63, 35131, Padova, Italy.

events and is not affected by static objects. In this work, we found it to be a robust feature for environment independent HAR. In principle, the Doppler shift can be effectively extracted from complex-valued CSI data. However, the CSI estimates gathered from COTS WiFi devices suffer from phase offsets that need to be corrected. For this reason, we also propose a new approach to obtain a clean version of the phase, that can be used to obtain the Doppler information.

The present work sharply departs from the literature on HAR with WiFi devices, as follows.

- We exploit the recently released Nexmon CSI-extractor tool to obtain data from an IEEE 802.11ac router operating on an 80 MHz frequency band, and with four antennas [10]. Former approaches rely on IEEE 802.11n devices (up to 40 MHz channels).
- We propose an original method for CSI phase correction. The algorithm is independently used at each receiving antenna without the need for a reference stream. Hence, the space diversity provided by the receiving antennas can be fully exploited for sensing purposes.
- We design an environment- and person-independent framework for HAR, which exploits the Doppler effect caused by moving humans. The information collected at the four monitoring antennas is combined to identify the activity, regardless of the user's position in the monitored area. Our approach is learning based, and reaches an average accuracy higher than 95% in the identification of four activities, namely walking, running, jumping and sitting, in the most challenging scenario, i.e., when the person, the day and the environment change with respect to those in the training set.

The rest of the paper is organized as follows. The related work is reviewed in Section II. In Section III and Section IV, we respectively detail the processing on the CSI data and the learning architecture for HAR. The experimental setup is presented in Section V, while the performance of the proposed approach is evaluated in Section VI. Conclusions are drawn in Section VII. For completeness, we include Appendix A and Appendix B, which provide an overview of the OFDM WiFi channel model, and the derivation of the Doppler information.

## II. RELATED WORK

### A. CSI based human activity recognition

HAR through CSI data from COTS WiFi devices was first studied in, e.g., E-eyes [11], CARM [12]. More recently, several articles showed the effectiveness of machine learning techniques in building algorithms that distinguish human activities based on CSI features [13]–[19]. However, these works do not focus on the robustness to environmental changes and on the generalization capability to previously unseen environments and subjects, which are key enablers for the successful development of WiFi-based sensing systems [9]. Only a few works try to address these weaknesses. In [20], the authors use a neural network based approach to extract environment-independent features from the CSI amplitude to recognize human movements. The performance of their algorithm is promising, but remains below 80% in the best scenario. In [21], transfer learning is shown to be effective

to adapt the WiFi-based HAR algorithm to different persons and days for the same environment. The algorithm presented in [22] leverages generative adversarial networks to generalize on new persons, while in [23] the matching network one-shot learning approach [24] is proposed to bridge the gap between previously seen environments and new ones. A recent work [25] addresses the problem of location and subject independent HAR through a learning architecture consisting of three deep neural networks. The algorithm is trained on the CSI amplitude collected by monitor routers placed in different positions inside a room, and is tested in the same room by changing the location of a single router. The approach presents a significant performance degradation when evaluated on other datasets (around 80% of accuracy).

To the best of our knowledge, no work in the literature proposes a solution that generalizes well on both unseen environments, days and subjects without any re-training step and using COTS devices. In the present work, we propose an effective solution to this problem, and we consider the popular DeepSense framework as a benchmark for comparison [13]. We selected DeepSense, as it is a very popular and widely adopted algorithm and considers an activity set similar to ours.

### B. Exploitation of the CFR phase

Some works, e.g., [26]–[28], consider a reference antenna and use the phase differences at the remaining ones to perform sensing. By construction, such phase difference is not affected by systematic offsets (same value across the antennas), but it is unable to cope with offsets that are antenna-specific. Exploiting a similar idea, in [29], the authors correct the rotation errors using a reference signal, obtained by connecting with a cable one of the available monitoring antennas with the transmitter. However, the need for a reference reduces the spatial diversity that can be exploited for sensing purposes at the monitor station. The possibility to remove the unwanted phase offsets without exploiting any reference is less addressed in the literature. In [30], the authors propose to mitigate the errors by considering the average signal over a number of time instants, while in [31] a two-step approach is presented to estimate and remove some of the antenna-independent offsets.

In this work, we correct the phase offsets by devising an optimization approach that finds the optimal CFR parameters from the raw channel data.

### C. Doppler based applications

A few works in the literature exploit the Doppler shift computed from WiFi CSI data. In [32]–[34], the Doppler information is used to track the movement of a user inside an environment. However, two different monitoring devices, placed in strategic positions, are used to obtain good estimates of the Doppler shift. A sensing system consisting of a single monitoring station is presented in [35], to recognize three different bodyweight exercises. In this work, the transmitter and the monitor stations must be placed in specific positions with respect to the user, so that the activity is performed perpendicularly to the radio link. Moreover, the detection algorithm is based on metrics that are manually extracted from

the raw CSI data and the Doppler trace. This makes the proposed approach highly activity-dependent, as the features are specifically designed to separate the three considered physical exercises. HAR through Doppler information has been recently addressed in [36]. The authors reach an high recognition accuracy (96%) on test data collected in the same environment where the algorithm is trained, proving the effectiveness of the Doppler information for HAR purposes. However, they do not provide any performance assessment in a different scenario.

### III. CSI DATA PROCESSING

WiFi systems adopt orthogonal frequency division multiplexing (OFDM), by transmitting the user information over  $M$  partially overlapping and orthogonal sub-channels, with  $M$  even. At the OFDM receiver, the channel parameters (amplitudes and phases) are continuously estimated for all the sub-carriers. This information is computed for each received packet based on known preamble symbols, and is collected by the CSI, a large (environment-dependent) complex matrix describing the channel frequency response (CFR) for each sub-channel along every spatial stream (antenna).<sup>1</sup>

For each pair of transmit and receive antennas, the CFR is a set of complex numbers  $A_m e^{j\phi_m}$  specifying the attenuation  $A_m$  and the phase shift  $\phi_m$  for each sub-carrier  $m \in \{-M/2, \dots, M/2 - 1\}$ . Considering a multi-path propagation channel, and using index  $p \in \{0, \dots, P-1\}$  to indicate the  $P$  copies of the transmitted signal that are collected at the receiver, the CFR estimated on packet  $n$  is written as

$$H_m(n) = A_m(n) e^{j\phi_m(n)} = \sum_{p=0}^{P-1} A_p(n) e^{-j2\pi(f_c+m/T)\tau_p(n)}, \quad (1)$$

where  $f_c$  is the main carrier frequency,  $T = 1/\Delta f$  is the OFDM symbol time, while  $A_p(n)$  and  $\tau_p(n)$  respectively represent the attenuation and the delay associated with path  $p$ . The complete OFDM model for the WiFi channel, along with a derivation of Eq. (1) are given in Appendix A.

In this work, the CFR matrix is estimated by a monitor WiFi device running the Nexmon CSI tool [37], as detailed in Section V. We remark that the collected CFR slightly deviates from the theoretical model in Eq. (1) due to hardware artifacts, which introduce an undesired phase offset  $\phi_{\text{offs}}$ , i.e.,

$$\bar{H}_m(n) = H_m(n) e^{j\phi_{\text{offs},m}}. \quad (2)$$

Next, we present the steps that we implemented to clean the CFR matrix that is extracted by the Nexmon CSI tool. Note that a new CFR matrix is retrieved for each received packet. Thus, the interval between subsequent acquisitions of the CFR is variable but, for the sake of exposition, in the following analysis we assume that a new sample is available every  $T_c$  seconds, with  $T_c$  fixed. We remark that, in a real WiFi network, the traffic exchanged between already deployed access points and user devices (e.g., streaming services), can be captured and exploited for HAR recognition purposes. When this is not possible, two WiFi access points are required to recreate the

<sup>1</sup>In the rest of the paper, the terms CSI and CFR will be used interchangeably.

setup, using a simple network controller to transmit packets at regular intervals and a second monitor device to infer the CFR from these.

#### A. Phase sanitization

The undesired phase offset  $\phi_{\text{offs},m}$  in Eq. (2) contains different contributions [29], [38], see Appendix A for their detailed explanation. Some of them, namely, the channel frequency offset (CFO), the phase-locked loop (PPO) and the phase ambiguity (PA), although changing in time have the same value across the sub-carriers in each spatial stream (receiving antenna). The sampling frequency offset (SFO) and the packet detection delay (PDD) are instead sub-carrier dependent. As shown in Appendix A, the offset  $\phi_{\text{offs},m}$  experienced at one receiving antenna in sub-channel  $m$  can be expressed as

$$\phi_{\text{offs},m} = -2\pi m(\tau_{\text{SFO}} + \tau_{\text{PDD}})/T + \phi_{\text{CFO}} + \phi_{\text{PPO}} + \phi_{\text{PA}}. \quad (3)$$

The main idea of our approach for phase sanitization is that the contribution of each path in Eq. (2) is affected by the same phase shift  $\phi_{\text{offs},m}$ . Hence, if we were able to separate the different paths, we could use (any) one of them as a reference to remove the phase offset from the CFR. In our method, the strongest path will be used to this end, as this is the path whose parameters are more reliably estimated at the receiver. The details are given shortly below. (Note that in the following analysis the time index  $n$  is omitted in the interest of readability.)

Let  $\mathbf{h}$  be the  $M$ -dimensional vector collecting the CFR information for the  $M$  sub-channels,

$$\mathbf{h} = [\bar{H}_{-M/2}, \dots, \bar{H}_0, \dots, \bar{H}_{M/2-1}]^T. \quad (4)$$

To separate the  $P$  multi-path contributions, we define a grid of  $P'$  possible paths with  $P' > P$  and solve a minimization problem to select the  $P$  components out of the  $P'$  ones that contribute to the CFR. We consider the following decomposition

$$\mathbf{h} = \mathbf{T}\mathbf{r}, \quad (5)$$

where  $\mathbf{T} = [\mathbf{T}_{-M/2} \dots \mathbf{T}_{M/2-1}]^T$  is an  $(M \times P')$ -dimensional matrix collecting the contributions to the CFR that depend on the sub-carrier index  $m$ , while  $\mathbf{r}$  is a  $P'$ -dimensional column vector representing the sub-carrier independent terms. The  $P'$ -dimensional row vectors  $\mathbf{T}_m$  are defined through a dictionary of candidate total delays  $\tau_{p,\text{tot}} = \tau_p + \tau_{\text{SFO}} + \tau_{\text{PDD}}$ , with  $p \in \{0, \dots, P' - 1\}$  as

$$\mathbf{T}_m = [e^{-j2\pi m \tau_{0,\text{tot}}/T} \dots e^{-j2\pi m \tau_{P'-1,\text{tot}}/T}], \quad (6)$$

The column vector  $\mathbf{r}$  can instead be modeled as

$$\mathbf{r} = e^{j(\phi_{\text{CFO}} + \phi_{\text{PPO}} + \phi_{\text{PA}})} \begin{bmatrix} A_0 e^{-j2\pi f_c \tau_0} \\ \vdots \\ A_{P'-1} e^{-j2\pi f_c \tau_{P'-1}} \end{bmatrix}, \quad (7)$$

and is obtained by solving the following minimization problem

$$\mathbf{P1} : \quad \mathbf{r} = \min_{\tilde{\mathbf{r}}} \|\mathbf{h} - \mathbf{T}\tilde{\mathbf{r}}\|_2 + \lambda \|\tilde{\mathbf{r}}\|_1. \quad (8)$$

The non-zero entries in the solution  $\mathbf{r}$  reveal the presence of a path  $p$  with corresponding total delay  $\tau_{p,\text{tot}}$ .

Using the decomposition in Eq. (5), vector  $\mathbf{r}$ , that we found solving problem **P1**, and Eq. (6), we are able to separate the contributions of the different paths in the CFR for each sub-carrier  $m$  by applying the following Hadamard product

$$\mathbf{X}_m = \mathbf{T}_m^T \circ \mathbf{r}. \quad (9)$$

$\mathbf{X}_m$  can be rewritten by replacing the terms in Eq. (9), as

$$\mathbf{X}_m = e^{-j2\pi m(\tau_{\text{SFO}} + \tau_{\text{PDD}})/T} e^{j(\phi_{\text{CFO}} + \phi_{\text{PPO}} + \phi_{\text{PA}})} \times \begin{bmatrix} A_0 e^{-j2\pi(f_c+m/T)\tau_0} \\ \vdots \\ A_{P'-1} e^{-j2\pi(f_c+m/T)\tau_{P'-1}} \end{bmatrix}. \quad (10)$$

At this point, we define  $p^* \in \{0, \dots, P' - 1\}$  as the position where  $\mathbf{r}$  has the highest amplitude, which, in turn, is associated with the strongest path. Let  $X_{m,p^*}$  be the  $p^*$ -th entry of  $\mathbf{X}_m$ . By multiplying  $\mathbf{X}_m$  by the complex conjugate of  $X_{m,p^*}$ , we remove the phase components that are constant across all the paths, including the offset, obtaining

$$\bar{\mathbf{X}}_m = A_{p^*} e^{j2\pi(f_c+m/T)\tau_{p^*}} \begin{bmatrix} A_0 e^{-j2\pi(f_c+m/T)\tau_0} \\ \vdots \\ A_{P'-1} e^{-j2\pi(f_c+m/T)\tau_{P'-1}} \end{bmatrix}. \quad (11)$$

Hence, summing up the elements of  $\bar{\mathbf{X}}_m$  (associated with the paths from  $p = 0$  to  $p = P' - 1$ ), we attain a CFR estimate for each of the sub-carriers, where the phase offset is mitigated, as follows,

$$\begin{aligned} \hat{H}_m &= \hat{A}_m(n) e^{j\hat{\phi}_m(n)} \\ &= A_{p^*} \sum_{p=0}^{P'-1} A_p e^{-j2\pi(f_c+m/T)\hat{\tau}_p} \\ &\simeq A_{p^*} e^{j2\pi(f_c+m/T)\tau_{p^*}} H_m, \end{aligned} \quad (12)$$

where  $\hat{\tau}_p = \tau_p - \tau_{p^*}$ . Note that  $\hat{H}_m$  of Eq. (12) represents the CFR estimate for sub-carrier  $m$ , where the phase offset has been removed and the contribution of each path is modulated according to the amplitude and phase of path  $p^*$ .

### B. Doppler trace computation

Fig. 1 shows how the amplitude and the phase change during a time interval of 3 seconds in two different scenarios, i.e., an empty room (on the left) and a room with a moving person (right plots). The presence of a human induces changes in the extracted channel parameters, which can be exploited by HAR algorithms. However, the CFR is affected by the whole indoor multi-path propagation environment and hence also accounts for the reflections from static objects. The reflected signals combine differently at each sub-carrier, and the delays induce sub-carrier specific phase shifts (see Eq. (1)). Such a behavior is *environment-specific* and is clearly identifiable in the amplitude plots of Fig. 1 (see the horizontal patterns in the figure). This fact does not allow developing robust algorithms for HAR that generalize across different environments, as the CFR is strongly affected by the room configuration itself (static objects, including walls, and the room shape). Also,

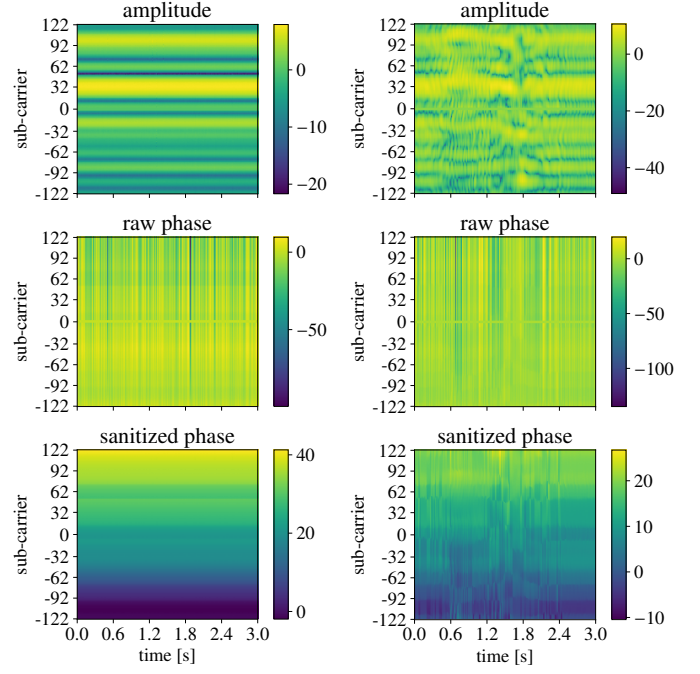


Fig. 1: Amplitude (in dB scale), raw and sanitized phases (unwrapped) of CSI data for an empty room (left plots) and with a person running (right plots). Each trace is three seconds long and shows the behavior on each of the monitored sub-channels (y-axis). Note that CSI is not available on the three central sub-carriers, see Section V for details.

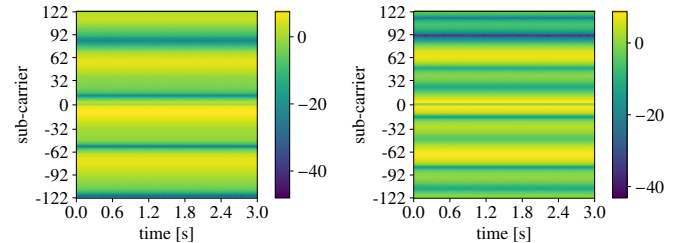


Fig. 2: CSI amplitude (dB scale) collected in the same empty room but in two different days. Environmental variations from one day to another change the multi-path channel response.

even considering the same indoor space, slight changes in the position of the objects therein have a non-negligible effect on the measured CFR, thus making the HAR task more challenging. As an example, Fig. 2 shows the CFR amplitude collected in two different days within the same empty room.

Due to these facts, in our framework we exploit the Doppler effect to obtain effective features for environment-independent HAR. The Doppler effect corresponds to a shift in the signal phase measured at the receiver as the geometry of the multi-path propagation changes during a transmission event. The movements of the scatterers cause variations in the time taken for the signal to reach the receiver through each of the propagation paths. This reflects in a phase shift in the received OFDM signal and, in turn, in the CFR matrix (see Appendix A

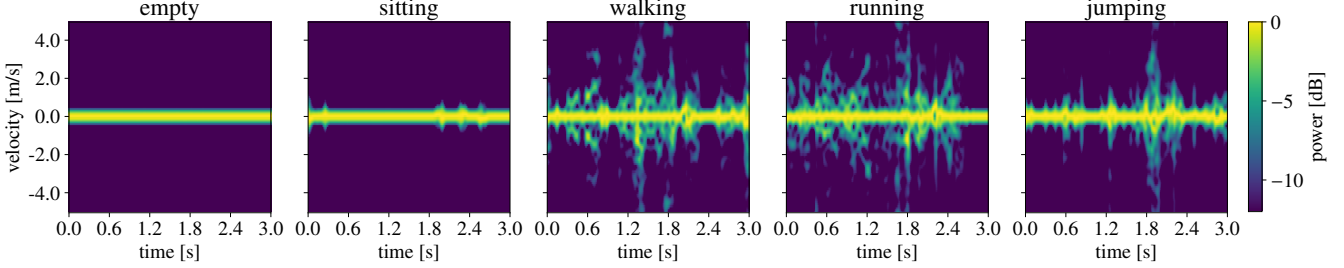


Fig. 3: Doppler traces related to five different setups (from left to right: empty room, sitting, walking, running and jumping). The velocity can be positive or negative depending on the way the scattering points move, changing the geometry of the multi-path propagation channel.

for a description of the OFDM model). Considering a path  $p$ , its associated delay,  $\tau_p(n)$ , can be expressed as the sum of two contributions. Let  $\ell_p$  be the path length related to the initial position of the scattering point and  $\Delta_p(n)$  be the delta caused by the movement of the point during the transmission period  $nT_c$ . We have that

$$\tau_p(n) = \frac{\ell_p + \Delta_p(n)}{c}, \quad (13)$$

with

$$\Delta_p(n) = - \int_0^{nT_c} v_p(x) \cos \alpha_p(x) dx, \quad (14)$$

where  $v_p$  indicates the speed of scatterer  $p$ , while  $\cos \alpha_p$  results from the combination of sinusoidal functions related to the angles of motion of the scatterer, and the angles of arrival and departure of the signal.

The activity-related movements of a human cause complex variations in the phase, as each body part acts as a scatterer moving at a specific velocity  $v_p(x)$ . This is revealed by the Doppler vector computed from the CFR matrix through a short-time Fourier transform over  $N$  subsequent channel estimates, i.e., during a *channel observation window*. These  $N$  estimates are respectively acquired by extracting the CFR matrix at the WiFi monitor for  $N$  subsequent packets, collected with sampling period  $T_c$ . The value of  $N$  is selected so that the attenuation, the velocities, and the angles can be considered fixed during the  $i$ -th observation window  $[iNT_c, (i+1)NT_c]$ , with  $i \geq 0$ . This allows us to rewrite  $\Delta_p(n)$  (Eq. (14)) as

$$\Delta_p(n) = -v_p \cos \alpha_p n T_c. \quad (15)$$

We define  $\mathbf{H}_i$  as the  $M \times N$  dimensional CFR matrix associated with the  $i$ -th observation window,

$$\mathbf{H}_i = \begin{bmatrix} \hat{H}_{-M/2}(iN) & \dots & \hat{H}_{-M/2}((i+1)N-1) \\ \vdots & & \\ \hat{H}_{M/2-1}(iN) & \dots & \hat{H}_{M/2-1}((i+1)N-1) \end{bmatrix}, \quad (16)$$

where the row and column indices respectively represent the OFDM sub-channels and the number of packets in the observation window.

At this point, each element of the  $N_D$ -dimensional Doppler vector  $\mathbf{D}_i = [d_i(-N_D/2), \dots, d_i(N_D/2-1)]^T$  is obtained as

$$d_i(u) = \sum_{m=-M/2}^{M/2-1} |\mathcal{F}\{\mathbf{H}_i\}(m, u)|^2, \quad (17)$$

where  $u \in \{-N_D/2, \dots, N_D/2-1\}$  and  $\mathcal{F}\{\cdot\}$  indicates the Fourier transform. For completeness, the mathematical expression for  $\mathcal{F}\{\mathbf{H}_i\}(m, u)$  is derived in Appendix B. The non-zero entries  $u$  in the Doppler vector reveal the presence of a scatterer with associated velocity

$$\hat{v}_p \cos \hat{\alpha}_p = \frac{uc}{f_c T_c N_D}, \quad (18)$$

where  $c$  is the speed of light.

In the remainder of this paper, we refer to Doppler trace as the matrix obtained by stacking a number of subsequent Doppler vectors, computed for consecutive observation windows.

As an example, in Fig. 3 we plot three-seconds long Doppler traces obtained as a person performs each of the four considered activities inside a room, compared with an empty room case. As expected, the Doppler trace related to the empty room only presents non-negligible power at the zero-velocity bin, revealing no movement in the environment. Instead, in the presence of a moving person the power is spread across different bins, reflecting the human-related multi-path changes.

#### IV. LEARNING ARCHITECTURE FOR HAR

The proposed HAR framework is conceived to fully exploit the data gathered from a commercial WiFi access point, i.e., using amplitude and phase information from the CFR, and combining this data for the available  $N_{\text{ant}}$  receiving antennas. Activity recognition is performed using  $N_w$  subsequent channel estimates at a time, which amounts to monitoring the channel for  $N_w T_c$  seconds. Note that this can be implemented in a sliding window fashion, thus updating the activity label at every new CSI sample.

The HAR algorithm consists of two steps.

- 1) First, we compute the Doppler traces from the data collected at all the receiving antennas and we use them to obtain activity estimates through a neural-network

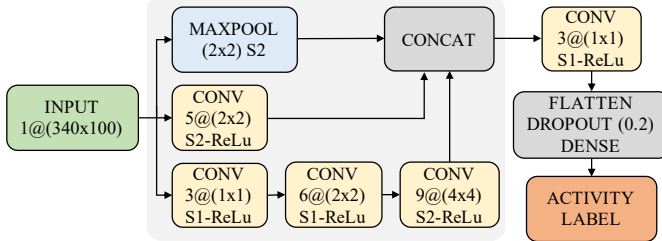


Fig. 4: HAR classification architecture for the single antenna system. The input of the network consists of 340 (about two seconds) long Doppler traces with 100 velocity bins. [CONV maps@(kernel)] blocks are convolutional filters with stride S#, followed by ReLu activation functions.

based algorithm (Section IV-A). Specifically, the machine learning based prediction chain that we build is *independently applied* to the data stream coming from each of the available antennas.

- 2) As a result of the previous step, we obtain  $N_{\text{ant}}$  independent predictions, one per antenna, which are combined, in a second step, through a decision fusion method that leads to the final activity estimate (Section IV-B).

We remark that an alternative approach that combines the data from the antennas (at the input of the above decision chains), would also be possible. Such combined input data (the Doppler traces coming from the antennas) would then be fed to a neural network to classify the activity. We experimentally verified that this is not a viable method to obtain an environment-invariant classifier, as the classification result depends on the antenna ordering and, in turn, on the person's location inside the room.

#### A. Activity classifier for the single antenna system

We framed the problem as a multi-class classification task with five classes (four user activities plus empty room), tackling it through a learning-based approach. The designed neural-network classifier takes as input the Doppler trace from a single antenna element, i.e., an  $N_w \times N_D$ -dimensional matrix obtained by stacking  $N_w$  subsequent Doppler vectors, and returns the label of the activity being performed. The classification architecture for the single-antenna system is shown in Fig. 4.

To start with, the input is fed to a simplified Inception module with dimensional reduction. This block extracts significant features from the Doppler trace at several scales by using layers with different kernel sizes in a parallel fashion. The structure is inspired by the reduction block proposed for the Inception-v4 neural network in [39], and consists of three branches combining max-pooling (MAXPOOL) and convolutional (CONV) layers. The  $N_w/2 \times N_D/2$  dimensional feature maps obtained at the output of each branch are concatenated and passed to the following convolutional filter with  $1 \times 1$  kernel, used to reduce the number of feature maps from 15 to 3. Hence, the output of such filter is flattened and passed to a fully connected (dense) layer with five output neurons, one for each activity class. The Dropout technique is used as a

regularization strategy, randomly zeroing 20% of the elements in the flattened vector preceding the dense layer. Overall, the proposed neural network has 128,535 parameters.

The classifier is trained in a supervised manner on data collected from a single indoor environment, using the cross-entropy loss function. The Doppler traces collected from the different antennas are used without any distinction among them, i.e., they are all added to a unique training set, without keeping track of the antenna that generated them. Using the trained architecture of Fig. 4, each input trace is associated with the activity having the highest score in the output five-dimensional vector, referred to as *activity vector*.

#### B. Decision fusion for the multiple antenna system

At runtime, the trained classification engine from the single antenna system is independently applied to the Doppler stream gathered by each antenna. This returns  $N_{\text{ant}}$  independent classification outcomes that are combined as we now explain. In detail, for each antenna we obtain a five-dimensional *activity vector* (the classifier output) and an *activity label*, corresponding to the largest element in the activity vector. When at least  $N_{\text{ant}} - 1$  activity labels agree on a certain activity, there is a clear winner, and the Doppler trace is associated with that activity. Otherwise, an overall *decision vector* is computed by summing, element-wise, the  $N_{\text{ant}}$  activity vectors. The trace is then associated with the activity having the highest score in this decision vector.

## V. EXPERIMENTAL SETUP

In this section we present the experimental setup designed for training and validating our HAR system. We first introduce the CSI extraction method (Section V-A), and then present the measurement scenarios and campaigns selected for building the dataset (Section V-B).

#### A. Nexmon extraction tool

Although most commercial WiFi chipsets can potentially generate CSI data, few manufacturers make this data available to developers and researchers, especially for modern chipsets. Hence, the majority of the WiFi-based HAR works in the literature have used outdated chipsets, for which some CSI extraction tools have been developed over the years: widely used ones are [40], [41], that target network interface cards implementing the IEEE 802.11n protocol. Recently, as part of the Nexmon project [37], [42], [43], it has been released a firmware patch allowing the extraction of CSI from specific Broadcom/Cypress WiFi chipsets.

In the present work, we use the Nexmon CSI extraction tool presented in [10] to obtain CSI data from an Asus RT-AC86U IEEE 802.11ac WiFi router. The extraction tool is compatible with the very-high-throughput mode, defined by IEEE 802.11ac, working with a total bandwidth of 80 MHz. Each CSI sample results in complex-valued channel information from 242 data sub-carriers for each transmit-receive antennas pair. In our experiments, with one transmitter antenna and four receiver ones, each CSI sample corresponds to four vectors of 242 complex values. Although the total number of sub-carriers

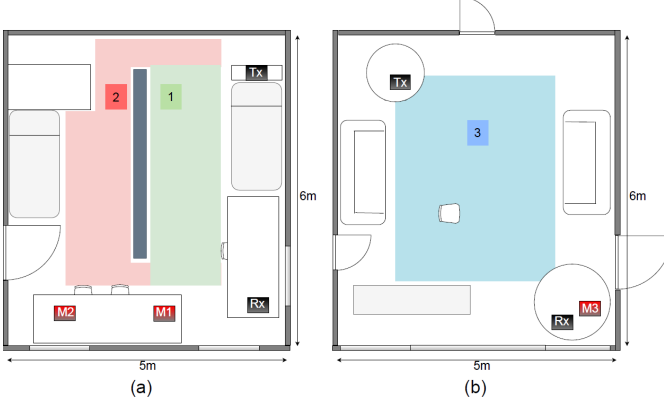


Fig. 5: Monitored environment for (a) sets  $S1 - S5$ , bedroom with a bookcase on the middle; (b) set  $S6$ , living room.  $Tx$  and  $Rx$  denote the transmitter and the receiver, respectively.  $M_j$ ,  $j \in \{1, 2, 3\}$ , denotes the monitor station.

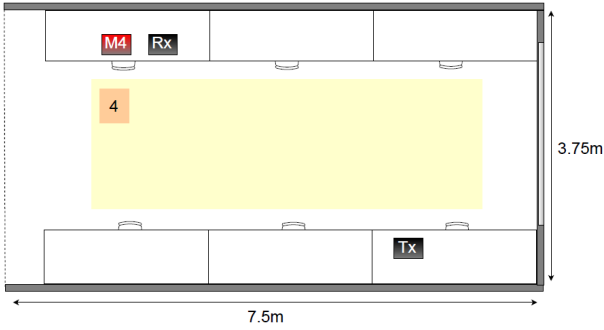


Fig. 6: Monitored environment for set  $S7$ . The desks are fully of computers and monitors.  $Tx$  and  $Rx$  denote the transmitter and the receiver, respectively.  $M4$  denotes the monitor station.

in 80 MHz is 256, each antenna vector has 242 components because the CFR is provided only for data sub-carriers, namely sub-carriers whose indexes are  $\{-122, \dots, -2\}$  and  $\{2, \dots, 122\}$ , i.e., no CFR value is provided for the control sub-carriers. Moreover, the values returned by the tool on the sub-carriers from  $-63$  to  $122$  need an inversion on the sign, probably due to hardware artifacts.

### B. Dataset acquisition and organization

In order to analyze the effects of different room geometries and static obstacles, we collected CSI samples in three different environments, a bedroom (Fig. 5-a), a living room (Fig. 5-b) and a University laboratory (Fig. 6), where one person moves within the area. Specifically, we obtain data from three volunteers (a male,  $P1$ , and two females,  $P2$ ,  $P3$ ) while they are walking or running around, jumping in place, or sitting somewhere in the room. The CSI samples are collected by a monitor node, implemented on an Asus router equipped with  $N_{ant} = 4$  antennas and running the Nexmon firmware. To generate the signals of opportunity exploited for sensing, we set up a WiFi transmission link using two Netgear X4S AC2600 WiFi routers, equipped with Qualcomm Atheros chipsets. The packets are transmitted through a single antenna, by using a fixed modulation and coding scheme (namely,

set	monitor position, $M_j$	person, $P_i$	direct path	type
$S1$	M1	P1	yes	train-test
$S2$	M1	P1	yes	test
$S3$	M1	P2	yes	test
$S4$	M2	P1	no	test
$S5$	M2	P2	no	test
$S6$	M3	P1	yes	test
$S7$	M4	P3	yes	test

TABLE I: Measurement conditions. For each set  $S_j$  we specify the position of the monitor station ( $M_j$ ) (see Fig. 5 and Fig. 6), the person ( $P_i$ ) performing the activity, and the presence of a direct path between the transmitter and the monitor. The last column indicates whether the set is used for training the proposed HAR algorithm or testing its performance.

MSC 4), by disenabling frame aggregation, and by setting the source rate to 173 packets per second. Since the Nexmon tool is configured for reading CSI samples on data packets only (i.e., by neglecting the acknowledgement frames sent by the receiver), a new channel estimate is generated every  $T_c \simeq 6 \times 10^{-3}$  s.

Fig. 5 and Fig. 6 display the positions of transmitter, receiver and monitor routers in the different environments. The black boxes represent the transmitter ( $Tx$ ) and the receiver ( $Rx$ ), while the red boxes labeled with  $M_j$  (with  $j \in \{1, \dots, 4\}$ ) indicate the position of the monitor station in different measurement sets. The activities are performed in the areas identified by a color and a number. Note that in the bedroom (Fig. 5-a), the direct path between  $Tx$  and  $M2$  is occluded by the bookcase in the middle of the room (grey rectangle in the figure).

We performed several measurement campaigns and we grouped them into seven sets,  $S_j$  with  $j \in \{1, \dots, 7\}$  each corresponding to a different triplet of environment-day-person. For each set, Table I provides the position of the monitoring station ( $M_j$ ), the area where the activities take place (identified by the color), and the person performing them ( $P_i$ ). We also include an indication of whether there is a direct path between the transmitter and the monitor stations. The configuration for sets  $S1-S2$  is the same apart from the day of measurement. Set  $S1$  is used to train the model, while set  $S2$  is used to test the generalization over different days. In  $S3$  we monitor the same environment as the previous sets, but in a different day and with a different person performing the activities. For sets  $S4$  and  $S5$ , the person is required to move in both area 1 and 2 of the bedroom depicted in Fig. 5-a. In these configurations, the direct path between the transmitter and the monitor is disturbed by the bookcase. Set  $S6-S7$  are collected in two different days and environments.  $S7$  represents the more challenging situation, in which no element (room, day, person) is in common with the scenario used for the training set.

Each measurement campaign involves 120 seconds of data for each activity, plus an additional trace of 120 seconds of data collected when the room is empty. Activities are repeated continuously by the volunteers during the trace acquisition time. The campaigns have been performed in different days through several months (April-December, 2020), resulting in a considerable time diversity. Overall, we collected nearly 120 minutes of CSI data, consisting of the CFRs estimated at all

communication and processing parameters	
monitored channel	IEEE 802.11ac 42
OFDM sample duration, $T$	$3.2 \times 10^{-6}$ s
modulation and coding scheme	MCS 4
channel estimates interval, $T_c$	$\simeq 6 \times 10^{-3}$ s
no. OFDM sub-channels, $M$	256 (245 used)
no. ch. estimates for Doppler computation, $N$	31
no. bins in a Doppler vector, $N_D$	100
no. Doppler vectors per classification window, $N_w$	340
no. monitoring antennas, $N_{\text{ant}}$	4

TABLE II: Summary of parameters related to the communication setup, and the Doppler traces computation.

the four antennas of the monitor station.

## VI. EXPERIMENTAL RESULTS

The HAR algorithm has been tested on the scenarios detailed in Table I. The adopted communication and processing parameters are summarized in Table II and are presented in Section VI-A. The performance is discussed in Section VI-B.

### A. Pre-processing steps and training

We considered some pre-processing operations for extracting the features of interest from the dataset. For each CSI sample, we divided the CFR values by the mean amplitude over the 242 monitored sub-carriers to remove unwanted amplifications. Then, the phase sanitization algorithm presented in Section III-A is applied. The CFR values on the three central sub-carriers are reconstructed together with the other 242 using Eq. (11), obtaining a CFR complex-valued vector (amplitudes and phases) of 245 components.

Doppler vectors are computed considering  $N = 31$  subsequent samples of the the sanitized CFR values. The velocity resolution is increased by zero-padding the signal out to  $N_D = 100$  points before applying the Fourier transform. A threshold is used on the resulting Doppler vectors to remove noisy contributions with power smaller than 12 dB. Finally, the Doppler trace acting as input features in our HAR system is built by stacking  $N_w = 340$  consecutive Doppler vectors. Doppler vectors are generated for each CSI acquisition by using a sliding window mechanism. Therefore, the complete Doppler trace lasts roughly  $340 \cdot T_c = 2$  s of measurements.

The HAR algorithm presented in Section IV has been trained by using the features extracted on set  $S1$ . More into details, 60% of data in  $S1$  composes the training set, while the remaining is evenly divided between validation and test sets. The other measurement sets,  $S2-S7$ , are only used in the test phase.

### B. HAR performance assessment

The classification accuracy and the F1-score obtained on each of the test sets are reported in the leftmost part of Table III. Note that, for  $S1$ , the evaluation is performed on the test set only, i.e., on new data never seen during training. Overall, the mean recognition accuracy is higher than 95%, reaching almost 100% when the environment and location of

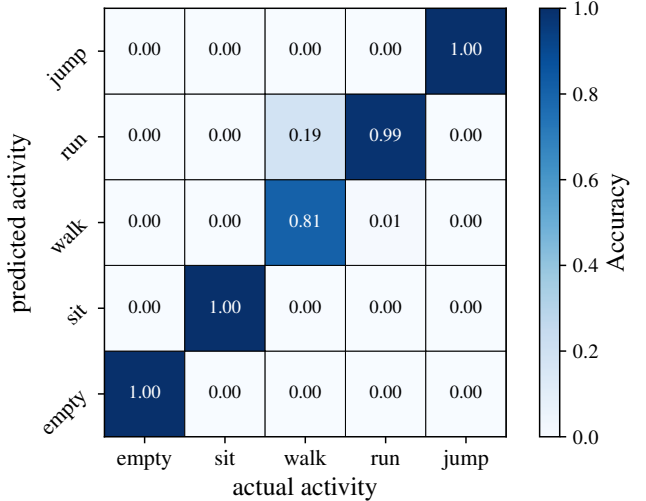


Fig. 7: Normalized confusion matrix for test set  $S7$ . Environment, day and person change with respect to the training.

the monitor node ( $M1$ ) remain the same of the training data, regardless of day of measurement and the person performing the activity ( $P1$  or  $P2$ ). We still obtain a good accuracy, around 97%, when the direct path between the transmitter and the monitor stations is blocked (sets  $S4$  and  $S5$ ). In this situation, the running activity is sometimes confused with the walking one, as revealed by the F1-score associated with these classes. However, this is a reasonable limit of our approach, as the activities are recognized by considering the velocity of different parts of the human body (i.e., the scattering sources), which can be very similar when people walk or run in indoor spaces. We also believe that a small confusion between the running and walking activities is admissible in almost all the fields of application of a WiFi sensing system. For example, in a residential scenario, it is more relevant to correctly distinguish between static and dynamic activities, rather than providing details about the type of movements.

For testing the generality of our algorithm under different environments, we consider the measurement sets  $S6$  and  $S7$ . When the person is the same of the training data, the average HAR accuracy approaches 100% while it decreases to 95.99% when both the person and the room change. Again, the lower accuracy is achieved for the walking activity, which is wrongly classified as the running one, as displayed in the normalized confusion matrix in Fig. 7.

On the rightmost part of Table III, we report the metrics obtained using the state-of-the-art DeepSense approach [13] in place of the single antenna classifier described in Section IV-A (i.e., before decision fusion). DeepSense relies on the sole CSI amplitude to perform HAR. A learning-based algorithm is used consisting of an encoder for feature extraction followed by a classifier. The encoder is trained as part of an auto-encoder structure to learn the most representative characteristics of the input signal. The code extracted by the amplitude trace is then processed by an activity classifier, which consists of convolutional and recurrent layers. Overall, the total number of parameters of DeepSense is comparable to the one used in

proposed approach												DeepSense [13]					
		empty	sitting	walking	running	jumping	mean		empty	sitting	walking	running	jumping	mean			
<i>S1</i>	accuracy (%)	100	100	100	100	97.93	<b>99.59</b>	<b>0.996</b>	100	100	100	99.62	98.26	<b>99.58</b>	<b>0.996</b>	<b>0.996</b>	
<i>S2</i>	accuracy (%)	100	100	100	99.28	99.64	<b>99.78</b>	<b>0.998</b>	0	86.34	75.56	32.11	83.58	<b>55.52</b>	<b>0.486</b>	<b>0.486</b>	
<i>S3</i>	accuracy (%)	100	100	96.64	100	100	<b>99.33</b>	<b>0.993</b>	97.45	96.33	79.60	22.59	9.44	<b>61.08</b>	<b>0.486</b>	<b>0.486</b>	
<i>S4</i>	accuracy (%)	100	100	99.84	93.27	94.63	<b>97.55</b>	<b>0.976</b>	0	84.05	64.83	43.80	37.10	<b>45.95</b>	<b>0.412</b>	<b>0.412</b>	
<i>S5</i>	accuracy (%)	100	100	98.58	84.93	99.45	<b>96.59</b>	<b>0.966</b>	0	99.12	49.78	47.27	17.76	<b>42.79</b>	<b>0.353</b>	<b>0.353</b>	
<i>S6</i>	accuracy (%)	99.76	100	100	100	99.20	<b>99.79</b>	<b>0.998</b>	0	87.99	49.70	26.92	49.08	<b>42.74</b>	<b>0.369</b>	<b>0.369</b>	
<i>S7</i>	accuracy (%)	100	100	81.24	98.71	100	<b>95.99</b>	<b>0.960</b>	100	66.81	8.49	99.77	34.59	<b>61.93</b>	<b>0.512</b>	<b>0.594</b>	

TABLE III: Performance of the proposed HAR strategy (on the left) compared with the state-of-the-art DeepSense approach (on the right). The accuracy and the F1-score are reported for each of the five classes together with their average value.

our approach. For performing a fair comparison, we trained DeepSense with the same portion of the set *S1* used for training our architecture. At run-time, the decision fusion approach in Section IV-B is applied to combine the output of the classifiers working on the single antenna data and obtain the final activity label. From Table III, we observe that the performance is in line with ours when considering the same environment of the training set, while degrades remarkably in all the other cases, even when data are collected in the same environment used for training, but in a different day (e.g., set *S2*). These results demonstrate that the sole amplitude information is insufficient to provide a good level of generalization across different situations. This is particularly evident for the identification of empty rooms, which in principle should be easily characterized by the lack of moving objects. DeepSense completely fails in identifying empty rooms in four out of the six sets *S2* – *S7*. Indeed, as shown and discussed in Section III, the CFR amplitude is environment-dependent and is also affected by small scene variations over days, such as changes in the positioning of the monitor node, room obstacles, and objects. Conversely, our HAR system generalizes across different days, environments and persons, especially for distinguishing between static and dynamic environments.

## VII. CONCLUDING REMARKS

In this work, a novel low-cost system for human activity recognition (HAR) in indoor spaces has been presented and experimentally validated. This system analyzes WiFi signals scattered into the environment and runs on COTS WiFi routers, which are usually available in indoor spaces for communication purposes, thus making the deployment and maintenance of an ad-hoc sensing infrastructure unnecessary. The use of WiFi routers as environmental sensors is enabled by the possibility of reliably estimating the wireless channel frequency response while receiving background data traffic.

In contrast with previous solutions, we implemented a robust HAR system, which does not require complex and

periodic calibrations, i.e., once trained, it can be used at run-time in a completely unseen situation. Our approach revolves around the idea of processing the CSI data gathered by a monitor access point to quantify the Doppler effect due to the presence of moving objects over time. Indeed, the Doppler shift describes the velocity of the scattering points (i.e., parts of the human body under movement), whose temporal trace depends on the specific activity and is neither affected by the environment geometry, nor by static objects. A learning based algorithm, working on the Doppler trace, has also been proposed to distinguish among different activities.

The robustness of the proposed HAR system has been challenged by conducting several measurement campaigns, using an IEEE 802.11ac router by Asus, operating on a frequency band of 80 MHz and having four antennas. Measurements are performed for seven different configurations of environment, access point position, people and day. Four human activities, i.e., sitting, walking, running and jumping are considered, together with the empty space recognition. Experimental results show that our system achieves a very high accuracy in all the considered scenarios: in the most challenging situation, when the person and the environment change with respect to those used at training time, the average accuracy is 96%. Moreover, the system outperforms state-of-art methods based on the analysis of the sole CSI amplitudes. Small errors are observed only when working with unseen persons and when distinguishing between walking and running. These errors somehow represent the fundamental limits of the approach, because they are due to the behavioral differences among different persons, or to the movement similarities in walking and running activities.

Future research avenues include the investigation of algorithms that work across differing hardware, at both the transmitter and the monitor access point, as well as the design of a new learning based algorithm that identifies multiple persons moving concurrently in the environment. Both extensions have important practical implications for real deployments and applications.

## APPENDIX A OFDM MODEL FOR THE WiFi CHANNEL

Next, we detail the main blocks of a WiFi transmission chain, deriving the expression for the CFR in Eq. (2).

### A. Transmitted signal model

In this subsection, we summarize how orthogonal frequency-division multiplexing (OFDM) is implemented by an IEEE 802.11 transmitter. OFDM uses a large number of closely spaced orthogonal sub-carrier, transmitted in parallel. Each sub-carrier is modulated with a conventional digital modulation scheme (such as QPSK, 16QAM, etc.).

The input bits are grouped and mapped onto source data symbols, which are complex numbers representing the modulation constellation points. Such constellation points are further grouped into  $M$  elements each, i.e., the OFDM symbols. OFDM symbols are then fed to an IFFT block that transforms the data prior to transmitting it over the wireless channel, in parallel, over  $M$  sub-channels with carriers spaced apart by  $\Delta f = 1/T$  Hz ( $T$  is the OFDM symbol time).

The duration of an OFDM symbol is  $\bar{T} = T + T_{\text{CP}}$ , where  $T_{\text{CP}}$  is the duration of the cyclic prefix, added to mitigate inter-symbol interference. Specifically, for IEEE 802.11ac the transmission bandwidth is 80 MHz, the samples are clocked out at 80 Msps, the number of sub-channels is  $M = 256$ ,  $T = 1/\Delta f = 3.2 \mu\text{s}$  (i.e.,  $\Delta f = 312.5 \text{ kHz}$ ),  $T_{\text{CP}} = 0.8 \mu\text{s}$ , and, in turn,  $\bar{T} = 4 \mu\text{s}$ .

Let  $\mathbf{a}_k = [a_{k,-M/2}, \dots, a_{k,M/2-1}]$  be  $k$ -th OFDM symbol, where  $a_{k,m}$  is the  $m$ -th OFDM sample. After digital to analog conversion, the baseband OFDM signal for the  $k$ -th symbol is

$$x_k(t) = \sum_{m=-M/2}^{M/2-1} a_{k,m} e^{j2\pi m t/T}, \quad (19)$$

where  $m \in \{-M/2, \dots, M/2 - 1\}$  is the sub-channel index. Considering  $K$  subsequent blocks, the baseband signal is

$$x(t) = \sum_{k=0}^{K-1} x_k(t) \xi(t - k\bar{T}), \quad (20)$$

with

$$\xi(t) = \begin{cases} 1 & \text{if } t \in [-T_{\text{CP}} - TM/2, TM/2] \\ 0 & \text{otherwise} \end{cases}, \quad (21)$$

and the signal transmitted over the WiFi channel is obtained by upconverting  $x(t)$  to the carrier frequency  $f_c$ ,

$$s_{\text{tx}}(t) = e^{j2\pi f_c t} x(t). \quad (22)$$

### B. Received signal model

At each receiver antenna,  $P$  signal copies are collected, due to the scatterers that the signal  $s_{\text{tx}}(t)$  encounters (multi-path propagation). Each path  $p$  is characterized by an attenuation

$A_p(t)$  and a delay  $\tau_p(t)$ . Neglecting the additive white Gaussian noise, the received signal  $s_{\text{rx}}(t)$  is written as

$$\begin{aligned} s_{\text{rx}}(t) &= \sum_{p=0}^{P-1} A_p(t) s_{\text{tx}}(t - \tau_p(t)) \\ &= e^{j2\pi f_c t} \sum_{p=0}^{P-1} A_p(t) e^{-j2\pi f_c \tau_p(t)} x(t - \tau_p(t)), \end{aligned} \quad (23)$$

and its baseband representation  $y_s(t)$  is expressed as,

$$y_s(t) = s_{\text{rx}}(t) e^{-j2\pi f_c t}. \quad (24)$$

A rectangular window  $[k\bar{T}, k\bar{T} + T]$  is used at the receiver to collect and decode the information carried by an OFDM symbol at a time. Without loss of generality, we assume  $k = 0$  and hence we omit such index from the following equations. The transmitted symbol  $a_m$  is recovered by computing the Fourier transform of the signal in the received window:

$$\begin{aligned} \hat{a}_m &= \int_{\bar{T}}^{\bar{T}+T} y(t) e^{-j2\pi m t/T} dt \\ &= \sum_{p=0}^{P-1} A_p e^{-j2\pi f_c \tau_p} \sum_{b=0}^{M-1} a_b e^{-j2\pi b \tau_p/T} \times \\ &\quad \times \int_{\bar{T}}^{\bar{T}+T} e^{j2\pi(b-m)t/T} dt \\ &= a_m T \sum_{p=0}^{P-1} A_p e^{-j2\pi(f_c + m/T)\tau_p}, \end{aligned} \quad (25)$$

where the sum in the last line corresponds to the frequency response of the WiFi channel,

$$H_m = \sum_{p=0}^{P-1} A_p e^{-j2\pi(f_c + m/T)\tau_p}, \quad (26)$$

that is estimated based on the known preamble symbols. In Eq. (25), we consider that the path attenuation and delay remain constant over each window, i.e.,  $A_p(t) = A_p$  and  $\tau_p(t) = \tau_p$ . Also, exchanging the order of integration and summation is legitimate as we deal with finite quantities, and we used  $\int_{\bar{T}}^{\bar{T}+T} e^{j2\pi(b-m)t/T} dt = 0$  if  $m \neq b$ .

### C. Phase offsets in the WiFi channel estimates

Hardware artifacts make the CFR gathered from WiFi devices slightly deviate from the model in Eq. (26). These artifacts introduce offsets (rotation errors) in the phase information, among which the most significant are [29], [38]:

- *carrier frequency offset (CFO)*, due to the difference between the carrier frequency of the transmitted signal and the one measured at the receiver. The CFO is only partially compensated for at the receiver [31].
- *sampling frequency offset (SFO)*, due to the imperfect synchronization of the clocks between transmitter and receiver.
- *packet detection delay (PDD)*, due to the time required to recover the transmitted modulated symbols from the received signal [31].

- *phase-locked loop phase offset (PPO)*, due to the phase-locked loop (PLL), the entity responsible for randomly generating the initial phase at the transmitter.
- *phase ambiguity (PA)*, due to the phase difference (multiples of  $\pi$ ) between the antennas, that in static conditions should remain constant.

Considering these contributions, the complete expression for the phase of the  $p$ -th path in the received signal is

$$\begin{aligned}\bar{\phi}_{p,m} = & -2\pi(f_c + m/T)\tau_p + \phi_{\text{CFO}} \\ & - 2\pi m(\tau_{\text{SFO}} + \tau_{\text{PDD}})/T \\ & + \phi_{\text{PPO}} + \phi_{\text{PA}}.\end{aligned}\quad (27)$$

Note that, while the CFO, SFO and PDD contributions take the same value across different antennas, the initial PLL phase (PPO) and PA are antenna specific [44], [45].

## APPENDIX B DERIVATION OF EQ. (17)

In the following Eq. (28), we derive the expression of  $\mathcal{F}\{\mathbf{H}_i\}(m, u)$ , where  $\mathbf{H}_i$  is the  $M \times N$  dimensional matrix in Eq. (16), collecting  $N$  subsequent channel estimates for each of the  $M$  sub-channels, and  $\mathcal{F}\{\cdot\}$  indicates the Fourier transform. According to the formulation in Section III, element  $m, n$  of  $\mathbf{H}_i$  is  $\hat{H}_m(n)$ . The models for the channel frequency response and the Doppler effect used in the computation are given in Eq. (12), Eq. (13) and Eq. (15), while  $W_m$  is the Hanning function, selected for the windowing operation. The term  $e^{j2\pi(m\hat{v}_p \cos \hat{\alpha}_p n T_c / T) / c}$  is negligible and omitted in the final expression. Note also that, to increase the velocity resolution, the signal can be zero-padded out to  $N_D$  samples before applying the Fourier transform.

$$\begin{aligned}\mathcal{F}\{\mathbf{H}_i\}(m, u) = & \sum_{n=0}^{N_D-1} \hat{H}_m(n) W_m(n) e^{-j2\pi n u / N_D} \\ \simeq & A_p \sum_{p=0}^{P'-1} A_p e^{-j2\pi(f_c + m/T)\hat{\ell}_p / c} \times \\ & \times \sum_{n=0}^{N_D-1} W_m(n) e^{j2\pi n(f_c \hat{v}_p \cos \hat{\alpha}_p T_c / c - u / N_D)}.\end{aligned}\quad (28)$$

## ACKNOWLEDGMENT

This work has been supported, in part, by the Italian Ministry of Education, University and Research (MIUR) through the initiative “Departments of Excellence” (Law 232/2016) and by the European Union’s Horizon 2020 programme under Grants No. 871249, project LOCUS. The views and opinions expressed in this work are those of the authors and do not necessarily reflect those of the funding institutions.

## REFERENCES

- [1] B. Dong, V. Prakash, F. Feng, and Z. O’Neill, “A review of smart building sensing system for better indoor environment control,” *Energy and Buildings*, vol. 199, pp. 29 – 46, 2019.
- [2] Y. Wang, S. Cang, and H. Yu, “A survey on wearable sensor modality centred human activity recognition in health care,” *Expert Systems with Applications*, vol. 137, pp. 167 – 190, 2019.
- [3] L. Minh Dang, K. Min, H. Wang, M. Jalil Piran, C. Hee Lee, and H. Moon, “Sensor-based and vision-based human activity recognition: A comprehensive survey,” *Pattern Recognition*, vol. 108, p. 107561, 2020.
- [4] J. Liu, G. Teng, and F. Hong, “Human activity sensing with wireless signals: A survey,” *Sensors*, vol. 20, no. 4, p. 1210, 2020.
- [5] J. Pegoraro, F. Meneghelli, and M. Rossi, “Multiperson continuous tracking and identification from mm-Wave micro-Doppler signatures,” *IEEE Transactions on Geoscience and Remote Sensing*, pp. 1–16, 2020.
- [6] F. Adib and D. Katabi, “See through walls with WiFi!” *SIGCOMM Comput. Commun. Rev.*, vol. 43, no. 4, p. 75–86, Aug. 2013.
- [7] B. Wang, Q. Xu, C. Chen, F. Zhang, and K. J. R. Liu, “The promise of radio analytics: A future paradigm of wireless positioning, tracking, and sensing,” *IEEE Signal Processing Magazine*, vol. 35, no. 3, pp. 59–80, 2018.
- [8] Y. He, Y. Chen, Y. Hu, and B. Zeng, “WiFi vision: Sensing, recognition, and detection with commodity MIMO-OFDM WiFi,” *IEEE Internet of Things Journal*, vol. 7, no. 9, pp. 8296–8317, 2020.
- [9] Y. Ma, G. Zhou, and S. Wang, “WiFi sensing with channel state information: A survey,” *ACM Computing Surveys*, vol. 52, no. 3, 2019.
- [10] F. Gringoli, M. Schulz, J. Link, and M. Hollick, “Free your CSI: A channel state information extraction platform for modern Wi-Fi chipsets,” in *Proceedings of the 13th International Workshop on Wireless Network Testbeds, Experimental Evaluation & Characterization (WiNTECH)*, Los Cabos, Mexico, Oct. 2019.
- [11] Y. Wang, J. Liu, Y. Chen, M. Gruteser, J. Yang, and H. Liu, “E-Eyes: Device-free location-oriented activity identification using fine-grained WiFi signatures,” in *Proceedings of the 20th Annual International Conference on Mobile Computing and Networking*, Maui, Hawaii, USA, 2014.
- [12] W. Wang, A. X. Liu, M. Shahzad, K. Ling, and S. Lu, “Understanding and modeling of WiFi signal based human activity recognition,” in *Proceedings of the 21st Annual International Conference on Mobile Computing and Networking*, New York, NY, USA, 2015.
- [13] H. Zou, Y. Zhou, J. Yang, H. Jiang, L. Xie, and C. J. Spanos, “DeepSense: Device-free human activity recognition via autoencoder long-term recurrent convolutional network,” in *Proceedings of the IEEE International Conference on Communications (ICC)*, Kansas City, MO, USA, 2018.
- [14] J. Ding and Y. Wang, “WiFi CSI-based human activity recognition using deep recurrent neural network,” *IEEE Access*, vol. 7, pp. 174 257–174 269, 2019.
- [15] Z. Shi, J. A. Zhang, R. Xu, and Q. Cheng, “Deep learning networks for human activity recognition with CSI correlation feature extraction,” in *Proceedings of the IEEE International Conference on Communications (ICC)*, Shanghai, China, 2019.
- [16] N. Damodaran and J. Schäfer, “Device free human activity recognition using WiFi channel state information,” in *Proceedings of the IEEE SmartWorld, Ubiquitous Intelligence Computing, Advanced Trusted Computing, Scalable Computing Communications, Cloud Big Data Computing, Internet of People and Smart City Innovation*, Leicester, United Kingdom, 2019.
- [17] N. Damodaran, E. Haruni, M. Kokhkarova, and J. Schäfer, “Device free human activity and fall recognition using WiFi channel state information (CSI),” *CCF Transaction on Pervasive Computing Interaction*, vol. 2, pp. 1–17, 2020.
- [18] T. Tegou, A. Papadopoulos, I. Kalamaras, K. Votis, and D. Tzovaras, “Using auditory features for WiFi channel state information activity recognition,” *SN computer science*, vol. 1, no. 3, 2020.
- [19] Z. Shi, J. A. Zhang, R. Xu, and Q. Cheng, “Deep learning networks for human activity recognition with CSI correlation feature extraction,” in *Proceedings of the IEEE International Conference on Communications (ICC)*, Shanghai, China, 2019.
- [20] W. Jiang, C. Miao, F. Ma, S. Yao, Y. Wang, Y. Yuan, H. Xue, C. Song, X. Ma, D. Koutsoukolas, W. Xu, and L. Su, “Towards environment independent device free human activity recognition,” in *Proceedings of the 24th Annual International Conference on Mobile Computing and Networking*, New York, NY, USA, 2018.
- [21] J. K. Brinke and N. Meratnia, “Scaling activity recognition using channel state information through convolutional neural networks and transfer learning,” in *Proceedings of the First International Workshop on Challenges in Artificial Intelligence and Machine Learning for Internet of Things*, ser. AIChallengIoT’19. New York, NY, USA: Association for Computing Machinery, 2019.
- [22] C. Xiao, D. Han, Y. Ma, and Z. Qin, “CsiGAN: Robust channel state information-based activity recognition with GANs,” *IEEE Internet of Things Journal*, vol. 6, no. 6, pp. 10 191–10 204, 2019.

[23] Z. Shi, J. A. Zhang, Y. D. R. Xu, and Q. Cheng, "Environment-robust device-free human activity recognition with channel-state-information enhancement and one-shot learning," *IEEE Transactions on Mobile Computing*, 2020.

[24] O. Vinyals, C. Blundell, T. Lillicrap, K. Kavukcuoglu, and D. Wierstra, "Matching networks for one shot learning," in *Proceedings of the Advances in Neural Information Processing Systems*, Barcelona, Spain, 2016.

[25] Y. Ma, S. Arshad, S. Muniraju, E. Torkildson, E. Rantala, K. Doppler, and G. Zhou, "Location- and person-independent activity recognition with WiFi, deep neural networks, and reinforcement learning," *ACM Trans. Internet Things*, vol. 2, no. 1, 2021.

[26] X. Wang, C. Yang, and S. Mao, "On CSI-based vital sign monitoring using commodity WiFi," *ACM Transactions on Computing for Healthcare*, vol. 1, no. 3, 2020.

[27] Y. Zeng, D. Wu, R. Gao, T. Gu, and D. Zhang, "FullBreathe: Full human respiration detection exploiting complementarity of CSI phase and amplitude of WiFi signals," *Proceedings of ACM on Interactive, Mobile, Wearable and Ubiquitous Technologies*, vol. 2, no. 3, 2018.

[28] D. Zhang, Y. Hu, Y. Chen, and B. Zeng, "BreathTrack: Tracking indoor human breath status via commodity WiFi," *IEEE Internet of Things Journal*, vol. 6, no. 2, pp. 3899–3911, 2019.

[29] N. Keerativoranan, A. Haniz, K. Saito, and J. I. Takada, "Mitigation of CSI temporal phase rotation with B2B calibration method for fine-grained motion detection analysis on commodity Wi-Fi devices," *Sensors (Basel)*, vol. 18, no. 11, p. 3795, 2018.

[30] A. Borhani and M. Pätzold, "RF-based human activity recognition: A non-stationary channel model incorporating the impact of phase distortions," in *Proceedings of the International Work-Conference on Artificial Neural Networks*, Gran Canaria, Spain, 2019.

[31] Y. Chen, X. Su, Y. Hu, and B. Zeng, "Residual carrier frequency offset estimation and compensation for commodity WiFi," *IEEE Transactions on Mobile Computing*, vol. 19, no. 12, pp. 2891 – 2902, 2019.

[32] X. Li, D. Zhang, Q. Lv, J. Xiong, S. Li, Y. Zhang, and H. Mei, "IndoTrack: Device-free indoor human tracking with commodity WiFi," *Proceedings of the ACM on Interactive, Mobile, Wearable and Ubiquitous Technologies*, vol. 1, no. 3, pp. 1–22, 2017.

[33] K. Qian, C. Wu, Z. Zhou, Y. Zheng, Z. Yang, and Y. Liu, "Inferring motion direction using commodity Wi-Fi for interactive exergames," in *Proceedings of the 2017 CHI Conference on Human Factors in Computing Systems*, Denver Colorado, USA, 2017.

[34] K. Qian, C. Wu, Z. Yang, Y. Liu, and K. Jamieson, "Widar: Decimeter-level passive tracking via velocity monitoring with commodity Wi-Fi," in *Proceedings of the 18th ACM International Symposium on Mobile Ad Hoc Networking and Computing*, Chennai, India, 2017.

[35] S. Li, X. Li, Q. Lv, G. Tian, and D. Zhang, "WiFi: Ubiquitous bodyweight exercise monitoring with commodity Wi-Fi device," in *Proceedings of the IEEE SmartWorld, Ubiquitous Intelligence & Computing, Advanced & Trusted Computing, Scalable Computing & Communications, Cloud & Big Data Computing, Internet of People and Smart City Innovation*, Guangzhou, China, 2018.

[36] M. Muaz, A. Chelli, A. A. Abdelgawwad, A. C. Mallofré, and M. Pätzold, "WiWeHAR: Multimodal human activity recognition using WiFi and wearable sensing modalities," *IEEE Access*, vol. 8, pp. 164 453–164 470, 2020.

[37] M. Schulz, D. Wegemer, and M. Hollick. (2017) *Nexmon: The C-based firmware patching framework*. [Online]. Available: <https://nexmon.org>

[38] H. Zhu, Y. Zhuo, Q. Liu, and S. Chang, "π-splicer: Perceiving accurate CSI phases with commodity WiFi devices," *IEEE Transactions on Mobile Computing*, vol. 17, no. 9, pp. 2155–2165, 2018.

[39] C. Szegedy, S. Ioffe, and V. Vanhoucke, "Inception-v4, Inception-ResNet and the impact of residual connections on learning," *CoRR*, 2016. [Online]. Available: <http://arxiv.org/abs/1602.07261>

[40] D. Halperin, W. Hu, A. Sheth, and D. Wetherall, "Tool release: Gathering 802.11n traces with channel state information," *ACM SIGCOMM Computer Communication Review (CCR)*, vol. 41, no. 1, p. 53, 2011.

[41] Y. Xie, Z. Li, and M. Li, "Precise power delay profiling with commodity WiFi," in *Proceedings of the 21st Annual International Conference on Mobile Computing and Networking*, New York, NY, USA, 2015.

[42] M. Schulz, D. Wegemer, and M. Hollick, "NexMon: A cookbook for firmware modifications on smartphones to enable monitor mode," Dec. 2015, arXiv:1601.07077.

[43] M. Schulz, J. Link, F. Gringoli, and M. Hollick, "Shadow WiFi: Teaching smartphones to transmit raw signals and to extract channel state information to implement practical covert channels over WiFi," in *Proceedings of the 16th Annual International Conference on Mobile Systems, Applications, and Services*, New York, NY, USA, 2018.

[44] A. Zubow, P. Gawlowicz, and F. Dressler, "On phase offsets of 802.11ac commodity WiFi," *arXiv preprint arXiv:2005.03755*, 2020.

[45] D. Zhang, Y. Hu, Y. Chen, and B. Zeng, "Calibrating phase offsets for commodity WiFi," *IEEE Systems Journal*, vol. 14, no. 1, pp. 661–664, 2020.



**Francesca Meneghelli** (Graduate Student Member, IEEE) received the B.Sc. degree in information engineering and the M.Sc. degree in telecommunication engineering from the University of Padova, Italy, in 2016 and 2018 respectively. She is currently pursuing the Ph.D. degree with the Department of Information Engineering at the same university. Her current research interests include deep-learning architectures and signal processing with application to remote radio frequency sensing and wireless networks. She was a recipient of the Best Student Paper Award at WUWNet 2016, the Best Student Presentation Award at the IEEE Italy Section SSIE 2019 and received an honorary mention in the 2019 IEEE ComSoc Student Competition.



**Domenico Garlisi** is CNIT researcher working at the University of Palermo. He received a Ph.D. degree in Engineering Electronic and Telecommunication at the University of Palermo, in 2014. He has been involved in several national and European research projects, he has worked on H2020 WiSHFUL project, H2020 Flex5Gware project and H2020 Symbiote project. He is involved in national project on IoT LPWAN. He has been a visiting researcher at the Department of Computer Science, UCLA, in 2013, working on wireless protocol optimizations for vehicular networks. His main research are related to wireless networks, software defined radio, sensor networks, vehicular networks and wireless systems for user localization and testing.



**Nicolò Dal Fabbro** received the B.Sc. degree in information engineering and the M.Sc. degree in ICT for internet and Multimedia from the University of Padova, Italy, in 2018 and 2020 respectively. He is currently pursuing the Ph.D. degree with the Department of Information Engineering at the University of Padova. His research interests are in machine learning, wireless sensing systems and edge computing.



**Ilenia Tinnirello** received her Ph.D. degree in telecommunications engineering from the University of Palermo in 2004. She is currently an Associate professor at the University of Palermo. She has also been Visiting Researcher at the Seoul National University, Korea, in 2004, and at the Nanyang Technological University of Singapore in 2006. Her research activities have been focused on wireless networks, and in particular on the design and prototyping of protocols and architectures for emerging reconfigurable wireless networks. I. Tinnirello has been involved in several European research projects.



**Michele Rossi** (Senior Member, IEEE) is a Full Professor of Telecommunications in the Department of Information Engineering (DEI) at the University of Padova (UNIPD), Italy, teaching courses within the Master's Degrees in ICT for internet and Multimedia at DEI (<http://mime.dei.unipd.it/>) and Data Science, offered by the Department of Mathematics (DM) at UNIPD (<https://datascience.math.unipd.it/>). Since 2017, he has been the Director of the DEI/IEEE Summer School of Information Engineering (<http://ssie.dei.unipd.it/>).

His research interests lie in wireless sensing systems, green mobile networks, edge and wearable computing. In recent years, he has been involved in several EU projects on IoT technology (e.g., IOT-A, project no. 257521), and has collaborated with companies such as DOCOMO (compressive dissemination and network coding for distributed wireless networks) and Worldsensing (optimized IoT solutions for smart cities). In 2014, he was the recipient of a SAMSUNG GRO award with a project entitled "Boosting Efficiency in Biometric Signal Processing for Smart Wearable Devices". In 2016-2018, he has been involved in the design of IoT protocols exploiting cognition and machine learning, as part of INTEL's Strategic Research Alliance (ISRA) R&D program. His research is currently supported by the European Commission through the H2020 projects SCAVENGE (no. 675891) on "green 5G networks", MINTS (no. 861222) on "mm-wave networking and sensing" and GREENEDGE (no. 953775) on "green edge computing for mobile networks" (project coordinator). Dr. Rossi has been the recipient of seven best paper awards from the IEEE and currently serves on the Editorial Boards of the IEEE Transactions on Mobile Computing, and of the Open Journal of the Communications Society.